Beamtests of ATLAS SCT Modules in August and October 2001

A.J.Barr [a], P.Cermak [d], Z.Dolezal [c], M.Donega [e], M.D'Onofrio [e], L.Eklund [b], J.E.Garcia Navarro [i], T.Horazdovsky [d], S.Kazi [g], P.Kodys [c], V.Linhart [d], G.F.Moorhead [g], P.W.Phillips [h], S.Pospisil [d], P.Reznicek [b], D.Saxon [f], M.Sinor [d], M.Solar [d], M.Vos [i], R.Wallny [b]

[a] *University of Cambridge, England*
[b] *CERN*
[c] *Charles University, Prague, Czech Republic*
[d] *Czech Technical University, Prague, Czech Republic*
[e] *University of Geneva, Switzerland*
[f] *University of Glasgow, Scotland*
[g] *University of Melbourne, Australia*
[h] *Rutherford Appleton Laboratory, England*
[i] *IFIC, University of Valencia/CSIC, Spain*

Abstract

We report on the beamtests of ATLAS Semiconductor Tracker (SCT) modules carried out at the ATLAS testbeam facility at the CERN SPS H8 beamline during August and October 2001. In all, 16 different modules were tested including 11 pre-production barrel modules, 4 "K4" prototype baseline endcap modules, and one "KB" prototype alternative endcap module. Of these, 5 had been previously irradiated with 24 GeV protons at the CERN PS T7 facility to the SCT reference fluence of 3×10^{14}p/cm^2. The efficiency, charge collection, spatial resolution and pulse shape were studied as functions of detector bias voltage, incidence angle and magnetic field. In addition, some detailed studies were made of the performance of the modules at the edges of the detectors and at the gaps between the detectors.

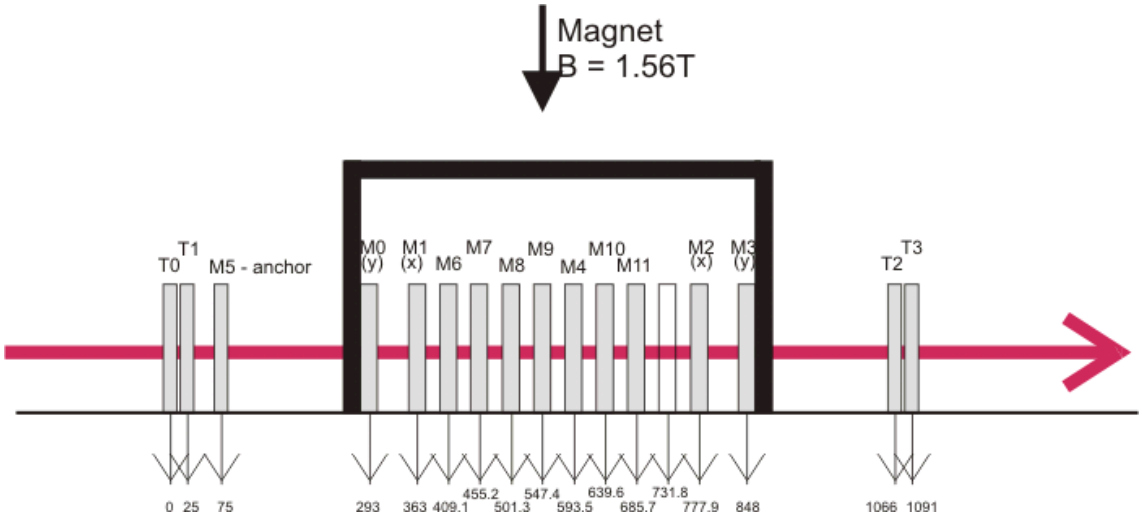

Fig. 1. A sketch of the layout of the beamline in October 2001. Modules T0-T3 are high resolution analogue silicon telescope with VA2 readout; modules M0-M3 are the SCT modules used as a binary telescope; modules M6-M11 are the modules under test. A similar arrangement, without the binary telescope, was used in August.

1 Setup

The ATLAS SCT beamtest setup at the H8 beamline at the CERN SPS in 2001 was very similar to that in 2000, described in detail in [3]. One change was the introduction this year of prototype SCT detector bias high voltage supplies in place of linear bench supplies. With these, both low and high voltage systems are close to those to be used in the real experiment. Clock, command and data transmission was electrical using the Mustard, Slog and SC2001 support card readout system.

The beam used throughout was the 180 GeV/c pion beam similar to previous years. The beam is well collimated at about 15 mm in cross-section, passing through a pair of scintillation counters which generate a trigger signal in coincidence. Upon receipt of the trigger a prompt busy is asserted preventing further triggers while the readout of the all event data fragments proceeds. Data fragments come from the Mustards, and also from the analogue telescope modules and from a TDC measuring the synchronisation delay between the random trigger and the LHC clock. Readout is event-by-event, the busy being released only when all fragments are read. In 2001 the SPS cycle was 16.8 seconds long with a spill of 4.8 seconds during which about 275 events were read. The beam intensity was typically 50,000 to 100,000 particles per spill.

2 Modules tested

The modules tested in August and October are summarised in tables 1 and 2. Modules were arranged such that those being directly compared were neighbouring where possible.

In August, the six barrel modules were all from the those assembled for the barrel module final design and production readiness reviews (FDR and PRR) in in Japan, England and Scandinavia. They were all built with ABCD3TA chips from wafers with the original epitaxial layer vendor ("old-epi"). Their hybrids were all of the K4 Kapton version on carbon-fibre substrates. Two of the modules had been irradiated with 24 GeV protons at the CERN PS T7 facility to a fluence of 3×10^{14}p/cm^2, the SCT standard fluence equivalent to an estimate of the worst case after 10 years in Atlas with a further safety margin. Following the irradiation, and before the beamtest, the modules underwent a controlled annealing for 7 days at 25°C. At other times between irradiation and beamtest the irradiated modules were, except for transportation, kept at low temperatures.

These six barrel modules therefore represented a good sample of near-final design at both extremes of radiation history. All six modules were mounted in identical test boxes with individual chilled liquid cooling. The temperatures quoted are typical of those measured by the hybrid thermistors under operating conditions.

Also in August, endcap modules built with K4 Endcap hybrids were beamtested for the first time. Three representative modules were tested including two of the long Outer type, one of of which had been irradiated, and one of the short Inner type. These therefore represented extremes of radiation history and strip length.

In October there were five barrel modules under test in a program designed to complement the August measurents. The five were again all from those built for the Barrel FDR/PRR, this time including four built with ABCD3TA chips from wafers with an epitaxial layer supplied by a new vendor ("new-epi"). The ABCD3TA production is proceeding with a large number of wafers from both the old and new epitaxial vendors, so both must be qualified. One module with old-epi chips tested in August, 0029, was included again to act as a control sample. Two of the new-epi modules had also been irradiated at the PS and annealed following the standard SCT irradiation protocol. A fourth endcap module included in October, 0048, was a first prototype of an alternative endcap design utilising barrel hybrids, a so-called "KB" module.

In addition, four other barrel modules were present in October. These were mounted in X-Y pairs in the most upstream and downstream positions avail-

Slot	*ID*	*Name*	*Module Type*	*Irradiated?*	*Hybrid Type*	*Chips*	*T (°C)*
0	0	0029	Barrel		B K4	ABCD3TA	-6
1	1	0018	Barrel		B K4	ABCD3TA	-7
2	2	0020	Barrel	*	B K4	ABCD3TA	-5
3	3	0037	Barrel	*	B K4	ABCD3TA	-4
4	4	0035	Barrel		B K4	ABCD3TA	-1
5	5	0036	Barrel		B K4	ABCD3TA	-7
6	6	K4_218	Endcap Outer	*	E K4	ABCD3TA	+4
7	7	K4_229	Endcap Inner		E K4	ABCD3TA	+25
8	8	K4_200	Endcap Outer		E K4	ABCD3TA	+11

Table 1
Modules in the August beamtest.

able to form a "binary telescope". The X modules were in standard slots, whereas the Y modules were mounted in newly arranged horizontal positions to measure the vertical coordinate. These modules did not participate in threshold scans but were kept at a fixed threshold of 1.2fC for reasonable efficiency and low noise occupancy. Two of the modules were from those tested in August, and two, with ABCD2T chips, from those tested in 2000. Such a binary telescope using SCT electronics with very fast shaping and pipelined, buffered readout allows tests at much higher beam intensities and trigger rates than is possible with the standard analogue telescope which has long-shaping time and slow multiplexed-readout VA2 chips. This is, however, at the expense of lower spatial resolution. The performance of the binary telescope and associated measurements will be reported in a separate note, [9].

3 Calibration

The calibration of the detector modules refers to the mapping of the threshold value of the comparator given by a DAC to its corresponding absolute charge scale. There is a well established procedure for deriving this conversion using the built in calibration circuitry in the ABCD3T/3TA [5] chip and the ROOT-based SCT module testing software package SCTDAQ [4]. The relation between the DAC value and the corresponding charge follows from a two step process. The bit-pattern in the DAC is converted to a voltage. This voltage is applied to a capacitor and the accumulated charge is injected in the front-end of the chip as if it had been collected in a silicon detector. To parametrise this

Slot	*ID*	*Name*	*Module Type*	*Irradiated?*	*Hybrid Type*	*Chips*	*T (°C)*
Y0	0	K3112	Barrel		B K?	ABCD2T	+4
0	1	0035	Barrel		B K4	ABCD3TA	-4
1	6	0046	Barrel		B K4	ABCD3TA New-epi	-7
2	7	0052	Barrel		B K5	ABCD3TA New-epi	-6
3	8	0047	Barrel	*	B K4	ABCD3TA New-epi	-8
4	9	0044	Barrel	*	B K4	ABCD3TA New-epi	-10
5	4	0029	Barrel		B K4	ABCD3TA	-8
6	10	0048	Endcap "KB"		B K4	ABCD3TA	-3
7	11	K4_211	Endcap Middle		E K4	ABCD3TA	+5
8		(vacant)					
9	2	0036	Barrel		B K4	ABCD3TA	-9
Y1	3	K3104	Barrel		B K?	ABCD2T	+3

Table 2
Modules in the October beamtest. In this beamtest, four modules were used to form a binary telescope. The first and last standard positions, 0 and 9, were occupied by two modules measuring the X coordinate, and two new positions upstream and downstream of these were occupied by modules placed at right-angles measuring the Y position (in notional slots labelled Y0 and Y1.) The other modules were all under test.

relation, a series of different charges is injected with the calibration circuitry and the comparator threshold is scanned to determine the 50% point for each injected charge. A typical example of the front-end response can be seen in Figure 2.

There are a number of uncertainties in the absolute charge scale. One originates from the uncertainty of the size of the calibration capacitor. This can to some extent be compensated for by correction factors derived from test structures on the silicon wafers, measured by the supplier as a step in their quality assurance procedure. The correction factors for the devices under test were all 1.13, except for module K4_200 for which it is 1.07. However, this only compensates for variations between production batches, not for variations within a batch. Some measurements of the calibration capacitor on individual wafers are also available. Table 3 in the results section lists the median charge results using the threshold correction factor obtained for the whole batch and using the individual wafer information. Charge differences of the order of 0.2 - 0.3 fC between identical modules remain in both cases. The global batch correction

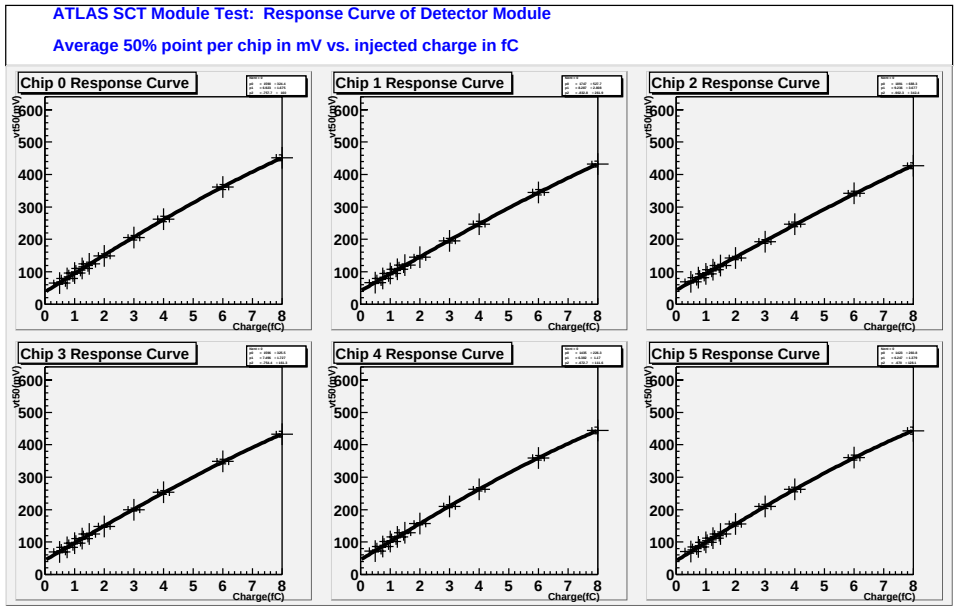

Fig. 2. The threshold of 50% occupancy is determined for each injected charge and the average 50% point per chip is plotted versus injected charge. Parameters for the mapping from threshold DAC value to corresponding charge are extracted from a fit to the data points.

factor has been used throughout the remainder of the note.

There are also uncertainties arising from the actual output value of the calibration circuit and threshold DAC. The DACs of the ABCD chip are slightly temperature dependent [6]. For a non-irradiated module the output voltage of the calibration DAC decreases in the order of 0.1% per °C. The corresponding number for the threshold DAC is 0.2% per °C. In view of this, the calibration for the beamtest are done in situ at operating temperature. As seen in Table 2 the temperature variations between the modules are insufficiently small for this effect to give any difference in module performance. However, some uncertainty of the absolute scale persists. The DACs in the front-end chips of course also suffer from radiation damage during the irradiation, and a difference in DAC output voltage has been seen between an irradiated and a non-irradiated module [6].

4 Measurement programs

The measurement programs for SCT beamtests are generally a series of similar threshold scans where each scan is a series of runs at certain nominal thresholds set using the previously established calibration relation. The standard threshold scan during 2001 consisted of an automated sequence of 16 runs,

each of 15000 events, at nominal charge settings 0.7, 0.8, 0.9, 1.0, 1.1, 1.2, 1.3, 1.5, 2.0, 2.5, 3.0, 3.5, 4.0, 4.5, 5.0, 6.0 fC. These cover the foreseen nominal operating region around 1.0 fC in some detail as well as the range well beyond the typical median charge.

Threshold scans were taken at each combination of parameters of interest - detector bias voltage, incidence angle (from 0 to a mechanical limit of about 15 degrees in either direction about an axis parallel to the vertical strips), magnetic field (off or on at 1.56 T), and position along or across the module as presented in the results below.

5 Alignment & tracks reconstruction

To evaluate the performance of the devices under test, one needs to be able to project the tracks with high precision. The internal alignment of the analog telescope and DUTs is very roughly limited by the mechanics of the test beam system. Detailed knowledge of relative positions and angles is obtained by a software alignment using the beam particle tracks. As a first step the reference frame is fixed by choosing two pairs of telescope planes and minimising the deviation of the tracks with respect to the Z-axis. All other planes are then aligned with respect to the first two by optimisation of the residuals. A more detailed description of the algorithm can be found in [3].

The alignment procedure is repeated every time a relevant parameter (angle, magnetic field etc.) is changed or any personnel access near the cold box occurs. This led to a total of 31 alignments. The `ascii` files containing the alignment information in the standard format can be obtained from the offline web pages [7].

Once the relative alignment is known, tracks can be reconstructed from the hit information in the analog telescope. The track projection is precise enough to resolve inter-strip effects like charge sharing.

For the August testbeam, the fraction of events with exactly one track with all four telescope XY points was typically around 50 %. This can be improved to nearly 80 % by accepting tracks with only three measured XY points in the sample from the four available telescope planes. The DSTs contains both types of tracks, allowing the choice either of high quality tracks or high statistics according to the need of the analysis. In the October run, new VA2 telescopes were used leading to a higher track reconstruction efficiency. The higher beam intensity, however, led to a significant fraction (up to 20 %) of multiple track events.

6 DST production

The raw data from all subdetectors are pre-processed into DSTs. These contain all information in an accessible format, with each data run corresponding to a ROOT TTree object. A description of the DST format and the C++ library can be obtained from the offline web pages [7].

DSTs for all August runs and runs 3767 to 3782 of the October beam test are available on the CERN high performance storage system CASTOR [8].

7 Results

Two important benchmarks for the module performance are the median collected charge and detection efficiency. Section 7.1 below reports on the results from measurements taken under "reference" conditions. The following sections discuss the effect of some relevant operating conditions on these results. The effect of a change in the bias voltage is discussed in section 10. Operation in a magnetic field and under non-perpendicular incidence are described in section 11. Section 12 studies possible edge effects, when the beam incides on the limits of the active area of the detector.

7.1 Reference conditions

To facilitate comparison with previous results, table 3 lists the response of the modules to perpendicularly incident particles without magnetic field. The detector bias voltage is set to its expected nominal value, 150 Volts for non-irradiated modules and 350 Volts for modules irradiated to 3×10^{14} p/cm^2. The efficiency is quoted at a corrected threshold of 1.0 fC, with the noise occupancy at the same threshold. Typical efficiency s-curves for an unirradiated and irradiated barrel module are shown in figure 3. Detailed plots for a number modules showing their efficiency and noise occupancy under reference conditions in the region around the nominal operating threshold are shown in figure 4.

The efficiencies are all over 99 %. The noise occupancies are very low for the non-irradiated barrel modules, consistent with laboratory measurements. Both irradiated barrel modules in the August test beam are within the noise occupancy specification. Identical modules built with chips from a different batch on a different epitaxial layer (the so-called new-epi chips) have a significantly higher noise occupancy. This confirms laboratory measurements. The K4_218

Module	TB	Eff (1fC)	NO (1fC)	Q_{med}	Q_c	S/N
0029	Aug	99.7	2×10^{-6}	3.21	3.21	14.4
0018	Aug	99.2	3×10^{-6}	3.28	3.22	14.8
0020*	Aug	99.6	4×10^{-4}	2.97	2.89	10.3
0037*	Aug	99.2	6×10^{-4}	2.67	2.62	8.7
0035	Aug	99.8	3×10^{-6}	3.60	3.54	15.4
0036	Aug	99.7	3×10^{-6}	3.53	3.47	15.5
K4_218*	Aug	99.6	8×10^{-4}	2.90	-	-
K4_229	Aug	99.6	2×10^{-6}	3.20	-	-
K4_200	Aug	99.7	5×10^{-4}	4.07(?)	-	-
0029	Oct	99.7	1×10^{-6}	3.26	3.26	14.8
0046	Oct	99.5	4×10^{-6}	3.31	-	14.8
0052	Oct	99.7	7×10^{-7}	3.37	-	14.0
0047*	Oct	99.7	3×10^{-3}	3.10	2.99	9.6
0044*	Oct	99.4	3×10^{-3}	3.07	3.02	10.1
0048	Oct	99.6	1×10^{-4}	3.28	-	11.2
K4_211	Oct	99.6	1×10^{-1}	3.15	-	-

Table 3
Summary of August and October reference results. All results correspond to the same runs, nominal bias (150/350 V), perpendicular incidence, no magnetic field. The column Q_{med} lists the median charge corrected by the global batch correction, whereas the results in column Q_c have been corrected by the factor obtained for the individual wafer.

irradiated end-cap module has a very reasonable noise performance. All other K4 end-cap modules suffered stability problems.

The median collected signal at nominal bias voltage varies significantly from one module to another. For non-irradiated barrel modules the charges range from 3.2 to 3.6 fC. The irradiated modules collect less charge when the detectors are biased to 350 Volts, between 2.7 and 3.10 fC. Correcting the charges on a wafer-by-wafer basis does not improve this spread significantly.

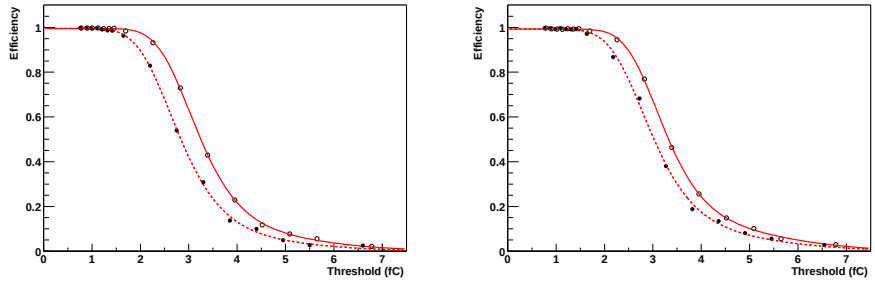

Fig. 3. Typical efficiency s-curves for irradiated *solid* and unirradiated *dashed* modules: *left* from August, modules 0029 and 0020*, and *right* from October, modules 0046 and 0047*.

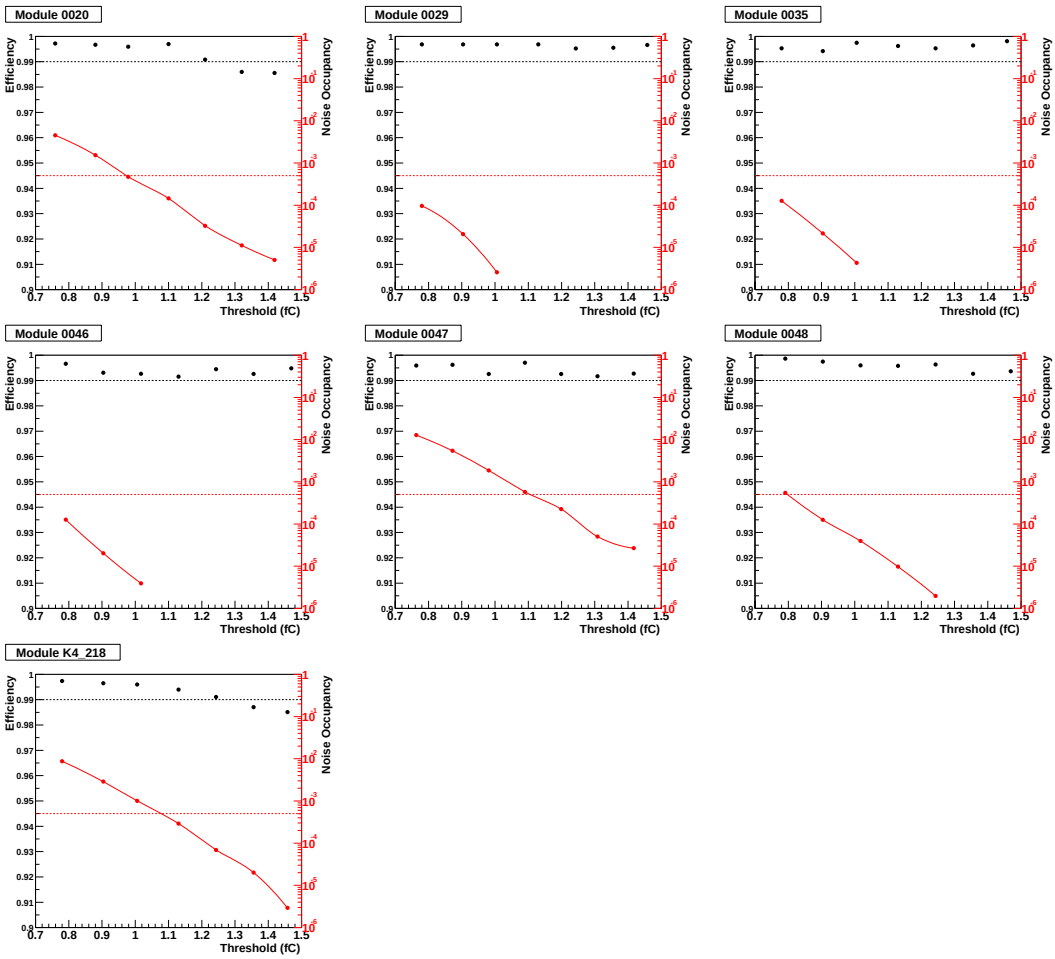

Fig. 4. Representative plots for a selection of modules under the reference conditions of the efficiency *(black, left axis)* and noise occupancy *(red, right axis)* versus corrected threshold in fC in the region near the nominal 1.0 fC operating point. The dashed lines indicate the module specifications for efficiency (99 %) and noise occupancy (5×10^{-4}) at the nominal operating threshold. Note also the operating margin in charge between the two specifications.

8 Inter-strip distribution

The good resolution of the analog telescope can be used to study the dependence of the efficiency on the inter-strip position of the track. Figure 5- 8 show the efficiency as a function of the reconstructed track position between two strips as fraction of the pitch for different values of threshold. Each step in the distribution is about 6 μm as set by the telescope track resolution. Both barrel and forward modules are presented.

If there is no charge sharing, all the charge carriers locally generated around the incident particle trajectory are collected on a single strip: with binary readout the Signal-to-Threshold is maximised in this condition. When the track crosses the detector between two strips, the released charge could be partially deposited on neighbouring strips (usually not more than 2 strips per cluster with perpendicular beam). There is observed an inefficiency around the middle inter-strip position where the charge sharing is greatest, decreasing the effective pulse height measured by the two single strips. This effect of charge sharing plays a role above 1.5 fC for intermediate values of threshold. A measure of its amount is the distribution of cluster size also as function of position between two strips (fraction of pitch) where a track hits the detector: the average number of strips involved increases in the central inter-strip position.

The spatial distribution of the collected charge has a gaussian shape that becomes narrower with increasing bias voltage. When the detector is fully depleted, charge collection is maximal and does not improve at higher voltages; it does, however, reduce the drift time and diffusion, so it can increase the number of single strip events. This effect is not observable since the pitch dimension is much larger than the σ of the charge distribution.

When a beam particle hits the detector with a non-perpendicular incident angle α, the charge sharing increases and the dip in efficiency *vs* inter-strip position becomes significant in a wide zone. Figure 7 shows a comparison of cluster size for irradiated and non-irradiated modules at different angles. Magnetic field also increases the charge sharing since it induces an angle on the released charge (Lorentz angle: see below section 11).

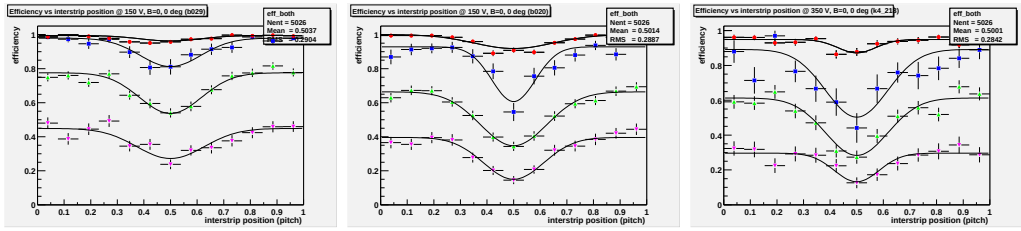

Fig. 5. B field OFF, perpendicular beam: Efficiency *vs* inter-strip position at four different thresholds (1.5, 2, 2.5 and 3 fC). *Left*: non-irradiated barrel module; *center*: irradiated barrel module; *right*: irradiated forward module.

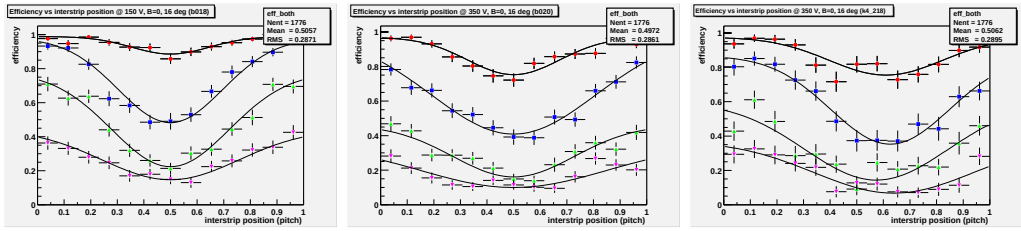

Fig. 6. B field OFF, beam with incident angle of 16°: Efficiency *vs* inter-strip position at four different thresholds (1.5, 2, 2.5 and 3 fC). *Left*: non-irradiated barrel module; *center*: irradiated barrel module; *right*: irradiated forward module.

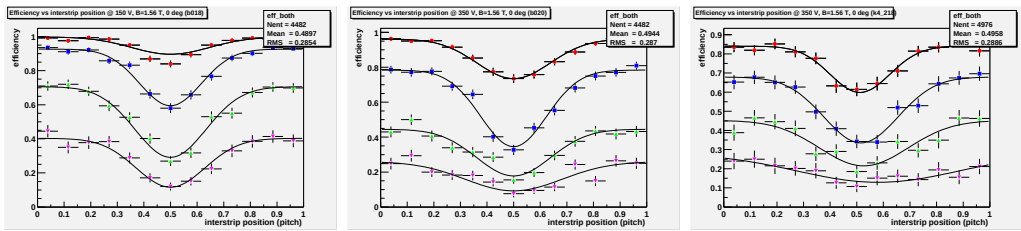

Fig. 7. B field ON, perpendicular beam: Efficiency *vs* inter-strip position at four different thresholds (1.5, 2, 2.5 and 3 fC). *Left*: non-irradiated barrel module; *center*: irradiated barrel module; *right*: irradiated forward module.

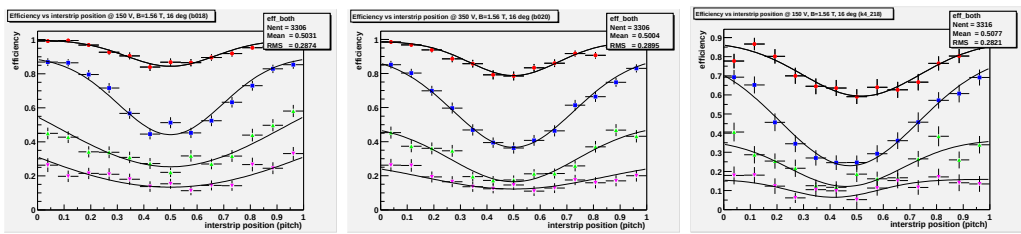

Fig. 8. B field ON, beam with incident angle of 16°: Efficiency *vs* inter-strip position at four different thresholds (1.5, 2, 2.5 and 3 fC). *Left*: non-irradiated barrel module; *center*: irradiated barrel module; *right*: irradiated forward module.

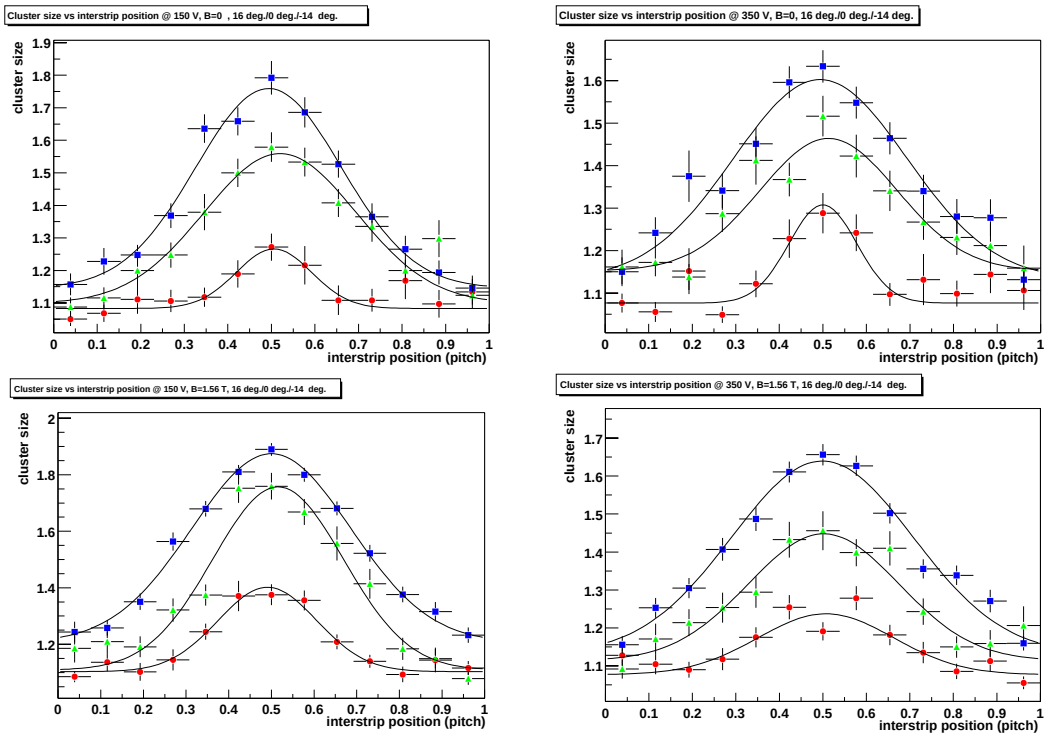

Fig. 9. Cluster size *vs* inter-strip position for different incident angle of the beam, without (top) and with magnetic field B=1.56 T (bottom): red circles are perpendicular beam, blue squares 16 degree angle, green triangles -14 degree angle. Non irradiated (right) and irradiated modules (left) are presented.

9 Spatial resolution

A fundamental issue for silicon strip detector is the spatial reconstruction capability. With a single strip, resolution in the rϕ plane) is the residual, calculated as the difference between where the track has crossed the centre of the silicon wafer (extrapolated from telescope system) and the centroid of the binary cluster. This value should be around pitch/$\sqrt{12}$, that for a barrel module is $\sim$ 23 μm and for an endcap depends on the track position since the pitch variates along the module. In a stereo module, where u and v are the fired strips in the two planes, the real spatial point could lie anywhere in the cross-hatched region showed in figure 10. Combination of a hit in each plane defines a parallelogram whose axis is rotated by half of an angle α as defined in the figure. Inside this region, the probability to find the space point coordinates is given by the triangular probability function. The corresponding resolution in $R\phi$ (perpendicular to the z axis as defined in the TDR) is:

$$\sigma_{\perp} = \frac{\sigma_1}{\sqrt{2} cos\frac{\alpha}{2}}$$

where $\sqrt{2}$ is a statistical term arising from two residual measurements σ_u and σ_v here assumed to be equal and denoted by σ_1. The resolution in z is

$$\sigma_{||} = \frac{\sigma_1}{\sqrt{2} sin\frac{\alpha}{2}} = \sigma_{\perp} cot\frac{\alpha}{2}$$

For barrel modules, where the strips are parallel, α is simply the stereo angle of 40 mrad; for forward module the situation is slightly more complicated, since we should combine the angles that come from rotation of each strip with respect to the line of symmetry. In both cases it is possible to consider the approximation for small α:

$$\sigma_{\perp} = \frac{\sigma_1}{\sqrt{2}}, \quad \sigma_{||} = \frac{\sqrt{2}\sigma_1}{\alpha}$$

In a test beam, the modules are perpendicular to the beam in both z and $R\phi$, so we redefine z as the beam axis and ($\perp$,||) as (x,y). This orientation of the coordinate system presents y along the direction of $\alpha/2$ as shown in figure 10 (u-v layout). X and y can be calculated from the u and v coordinates as:

$$x = \frac{u+v}{\sqrt{2} cos\frac{\alpha}{2}} \qquad y = \frac{v-u}{\sqrt{2} sin\frac{\alpha}{2}}.$$

Figure 11 shows resolutions for both barrel and forward modules at 1.5 fC threshold, with beam perpendicular and also at the maximum incident angle of 16 degrees.

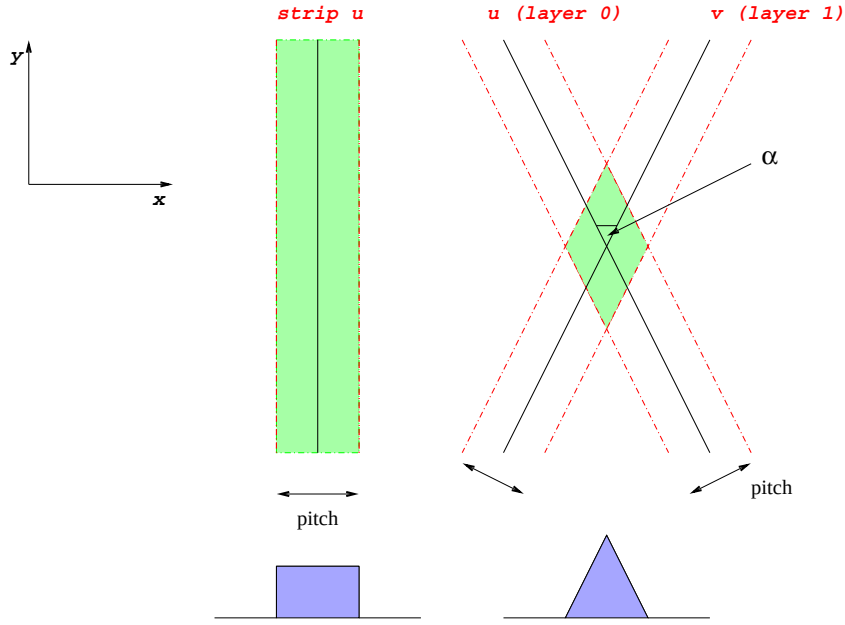

Fig. 10. Measurements given by (*Left*) a single strip and (*Right*) a stereo layer. In this case, for each plane one strip fires (u and v) and the real space point could lie anywhere in the parallelogram given by single strip resolution (residuals).

10 Bias voltage

The bias voltage of the detectors has a very strong effect on the signal of the modules. Below the depletion voltage, part of the detector does not contribute to the signal. Once the detector is fully depleted the field strength in the Silicon determines how fast charge collection occurs. In irradiated detectors, charge trapping may depend on the velocity of the carriers and thus the bias voltage. In the August testbeam measurements were performed at four different voltages around the nominal bias: 100, 150, 200 and 250 Volts for non-irradiated modules, and 300, 350, 400 and 450 Volts for irradiated modules. All of these voltages are thought to be above the full depletion voltage.

Figures 12 present median charge (left) and efficiency (right) as a function of bias voltage. Incidence was perpendicular for these measurements and no magnetic field was applied.

For the non-irradiated modules (round markers), the collected charge increases with bias in a way that is typical for ballistic deficit of the shaper. Below around 150 Volts charge collection becomes slow with respect to the peaking time of the shaper, leading to a loss of the charge. The efficiency is not affected

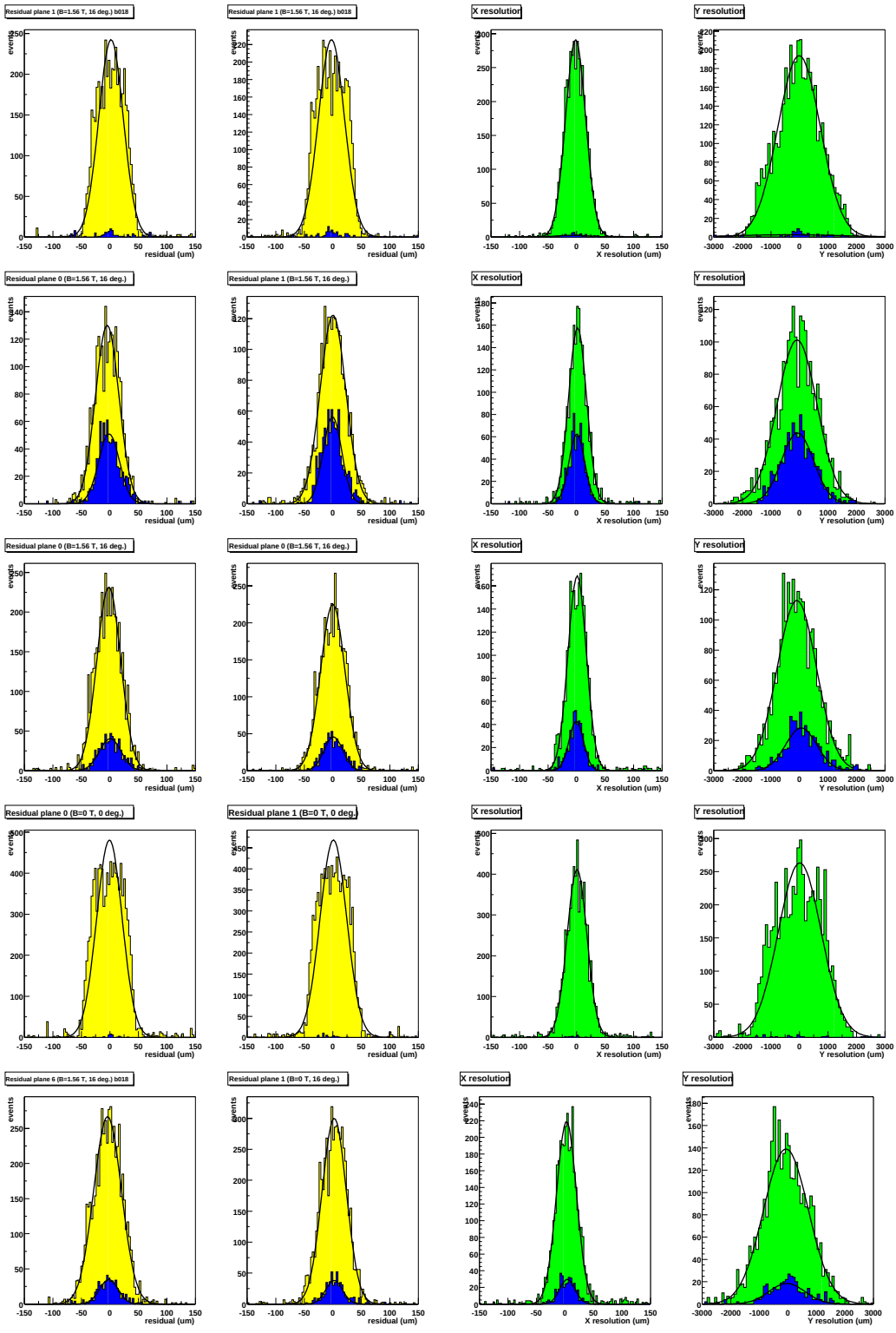

Fig. 11. Residuals in u,v and resolution in x,y for combination of single (light fill area) and double clusters (dark fill area) on both stereo planes. From top, non irradiated barrel module, B = 1.56 T, perpendicular incidence, non irradiated barrel module, B = 1.56 T, 16 degrees incidence, irradiated barrel module, B = 1.56 T, perpendicular incidence, irradiated forward module, B = 0 T, perpendicular incidence, irradiated forward module, B = 0 T, 16 degrees incidence.

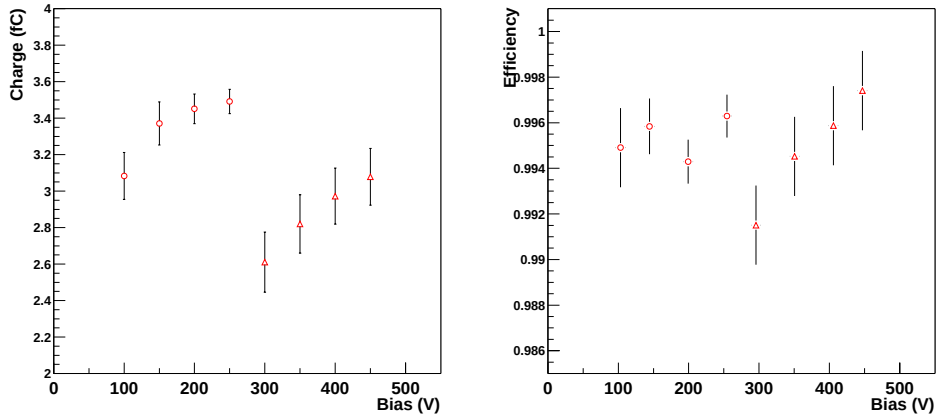

Fig. 12. Median charge vs bias voltage for barrel modules (left). Efficiency variation with voltage (right).

significantly, as in these conditions the modules have a quite large charge margin.

For the irradiated modules (triangular markers) the situation is more complicated. The collected charge is found to depend strongly on the bias voltage in the range under study. Even for the highest bias voltage, 450 Volts, the collected charge is lower than that found in non-irradiated modules. At least part of the charge loss is thought to be due to trapping of drifting carriers in radiation induced lattice defects. In this case, the charge loss at lower voltages is reflected in a slight bias voltage dependence of the efficiency at 1 fC, although the efficiency remains over 99% down to 300 Volts.

11 Magnetic field and incidence angle

An important subject of study in the test beam is the influence of magnetic field and incidence angle on the performance of the modules. Threshold scans were performed at various angles, both without magnetic field and in the 1.56 Tesla field of the Morpurgo magnet. This section will report on the dependence of the most important measures of the performance - efficiency at the operation threshold, median collected charge and spatial resolution - on the incidence angle and field.

To evaluate the effect of the incidence angle two cases have to be distinguished.

- A: The cylinder + end-caps geometry of ATLAS will lead to incidence angles up to 68 degrees for the last barrel on the inner cylinder and 34 degrees on the outer ring of the first disk. This case is equivalent to a rotation around

an axis in the detector plane, perpendicular to the readout strips.

- B: The track curvature in the solenoidal magnetic field leads to a smaller variation of the incidence angle in the perpendicular $(R-\phi)$ plane (up to some 10 degrees for a 1 GeV particle). Here the equivalent rotation axis is parallel to the strips.

For both cases the longer path length through the Silicon leads to an increase of the deposited charge by a factor $1/\cos\alpha$. An important difference is that in the latter case (B) the projection of the deposited charge on the strip plane is much broader. This situation is drawn in figure 14. In the binary readout scheme, charge sharing between neighbouring strips has a slight beneficial effect on the spatial resolution, but can lead to a loss of a significant fraction of the charge.

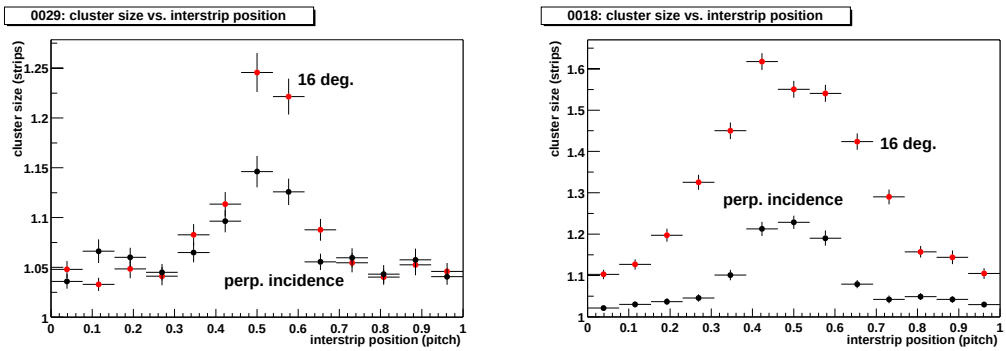

Fig. 13. Effect of the variation of the incidence angle in the two module orientations: module 0029 is placed vertically, equivalent to case A. Module 0018 is placed horizontally, equivalent to case B.

To illustrate the difference between both cases, we compare the effect of non-perpendicular incidence in two modules rotated according to A and B. Figure 13 shows the average cluster size - a measure for the amount of charge sharing - as a function of the position between two strips where the track hit the detector [1] . When incidence is perpendicular, both modules are identical. Charge sharing is only significant in a small region exactly between two strips. The second set of points in the same figure corresponds to the maximum rotation angle in this study, 16 degrees. In the module representing the former case A (0029) the increase in charge leads to a slight increase in average cluster size for the tracks in the center between two strips. In module 0018, however, both the height and width of the central peak have increased dramatically.

For the simpler situation of case A, one expects that the median collected charge increases linearly with the deposited charge, i.e. $Q \propto 1/cos\alpha$. The data

[1] in the case of non-perpendicular incidence ($\alpha \neq 0$) the position of the track with respect to the strips is determined as the projection of the track position in the center of the Silicon wafer

Link	Q_0	$Q_0/\cos 7$	Q_{7°	$Q_0/\cos 11.5$	$Q_{11.5^\circ}$	$Q_0/\cos 16$	Q_{16°
Both	3.19	3.21	3.22	3.25	3.29	3.32	3.33

Table 4
Measured median charges for different angles, module 0029.

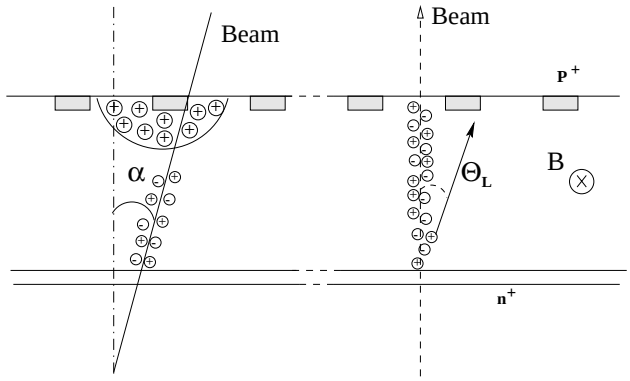

Fig. 14. Representation of the effect of the incidence angle and the application of a magnetic field.

from module 0029 in table 4 agree very well. Results from case B will be presented after a discussion of the effect of the magnetic field.

Strong magnetic fields can bend the path of the drifting charge carriers in the Silicon. For the barrel modules in the solenoidal field of the inner tracker volume the B field is parallel to the strips. In this configuration, the action of the magnetic field results in a deviation of the measured position. Figure 14 shows the equivalence of this effect to a rotation by a small angle $\Theta_L = \mu^H B = r_H \mu B$, where μ^H the Hall mobility, the conduction mobility μ multiplied by the Hall scattering factor r_H [10]. B is the magnetic field perpendicular to incident particles.

In the following, the combined effect of incidence angle (as in case B) and magnetic field will be discussed. Note that the relative orientations of the magnetic field and the rotation axis with respect to the modules is representative for barrel modules at $\eta = 0$.

A sensitive measure of charge sharing is the average cluster size. Here, the cluster size dependence on angle in a magnetic field will be used to determine the Lorentz angle. Noise clusters are excluded by placing a 200 micron window around the track position predicted by the telescope. Also, clusters are rejected when they fall outside the optimum time window. Figure 15 are the plots for

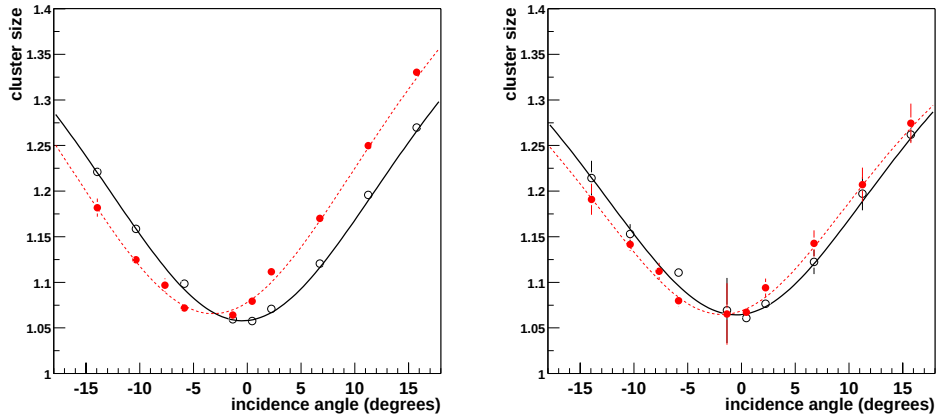

Fig. 15. Cluster size versus angle for non-irradiated modules at 1 fC (left) and irradiated at 1 fC (right). Filled markers are measurements with a magnetic field of 1.56 T, the open markers without field

all the modules with the fits to the data points.

In a more detailed analysis the Lorentz angle is determined independently for each module plane. The statistical error is taken to be the standard deviation of all the measurements for a set of modules. As a cross check, the fit results for angle zero have been calculated. The result $\Theta_L = 0.4° \pm 0.2°$ reflects the overall uncertainty in the angle scale. With this method the Lorentz angle is obtained for both groups: non-irradiated and irradiated modules.

$$\Theta_L(150V) = 3.3° \pm 0.3° \tag{1}$$

$$\Theta_L(350V) = 2.1° \pm 0.4° \tag{2}$$

As the irradiated modules are biased at a higher voltage, the observed difference could be due to an electric field dependence of the Lorentz angle or a change in the properties of the charge carriers due to irradiation. In the literature, the effect of proton irradiation on the mobility and thus Lorentz angle of holes is found to be compatible with no effect [11] [13] [14] or very small, of the order of 2% [12]. The difference in voltage, that is electric field inside the detector, has the effect of changing the Θ_L through the electric field dependence of the carrier mobility μ. Theoretical models applied to Beam Test conditions (silicon temperature $T = 261$ K, thickness $d = 285\mu$m and field $B = 1.56$ T), $\Theta_L(150\text{V}) = 3.3°$ and $\Theta_L(350\text{V}) = 2.4°$ [10] [11] predict values that agree within errors with our measurement.

Having established the Lorentz angles for irradiated and non-irradiated modules, the combined effect of magnetic field and non-perpendicular incidence on the module performance will be studied. This study includes all barrel modules except 0029. The modules are biased to nominal bias voltage: 150

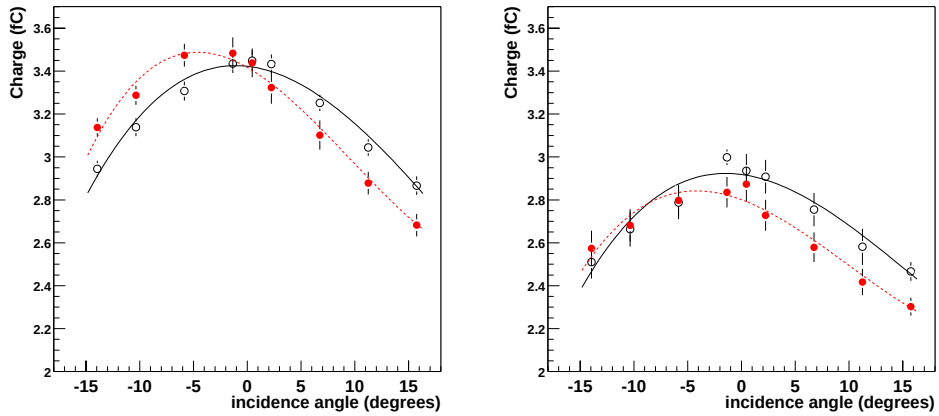

Fig. 16. Median charge versus angle for non-irradiated (left) and irradiated (right) modules. Filled marker are measurements in a 1.56 T magnetic field, open markers without field

Volts for non-irradiated modules, 350 Volts after receiving the full expected dose. Therefore, the modules are naturally classified in two groups: irradiated and non-irradiated modules. The results of modules belonging to one group are generally compatible within errors. Therefore, the results are presented as averages over all (non-) irradiated barrel modules, the errors representing the variation between different modules.

Figure 16 presents the median charge calculated for both groups of modules. The effect of charge sharing is bigger than the effect of the $(1/cos\alpha)$ path length increase, so for non-perpendicular incidence the observed charge decreases. The effect is similar in non-irradiated and irradiated modules, although the absolute values of the charges are quite lower in the irradiated modules. The magnetic field shifts the curve by a small amount, the Lorentz angle.

A significant charge loss may lead to a loss of efficiency, especially in modules that already had a reduced charge margin, i.e. irradiated modules. Figure 17 presents the efficiency at a threshold of 1 fC, the envisaged ATLAS working threshold, non-irradiated (left) and irradiated modules(right). Open markers represent measurements without magnetic field, the filled markers results in a 1.56 T field. The incidence angle has no significant effect on the efficiency at this threshold, both for non-irradiated and irradiated modules.

In case the noise of the electronics is higher than the specification the requirement on the noise occupancy forces the operating threshold up. Figure 18 shows the efficiency at a threshold of 1.2 fC.

As before no effect is observed in the non-irradiated modules, but now a clear

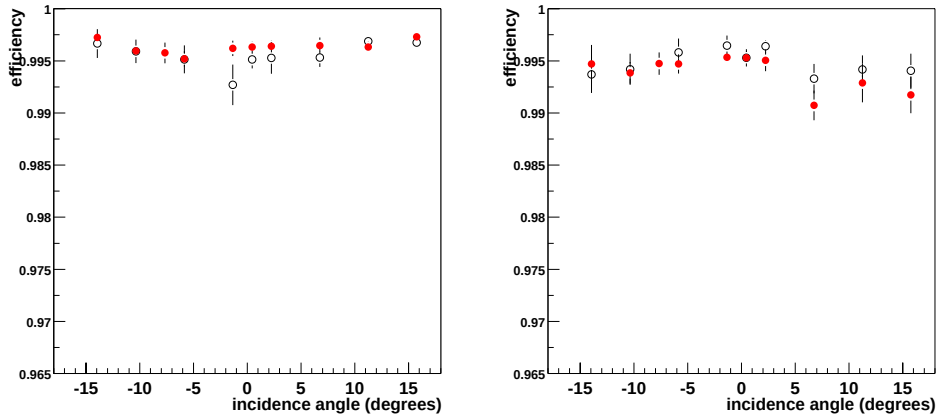

Fig. 17. Efficiency versus angle for non-irradiated modules at 1 fC (left) and irradiated at 1 fC (right). Filled markers are measurements in a 1.56 T magnetic field, open markers without field

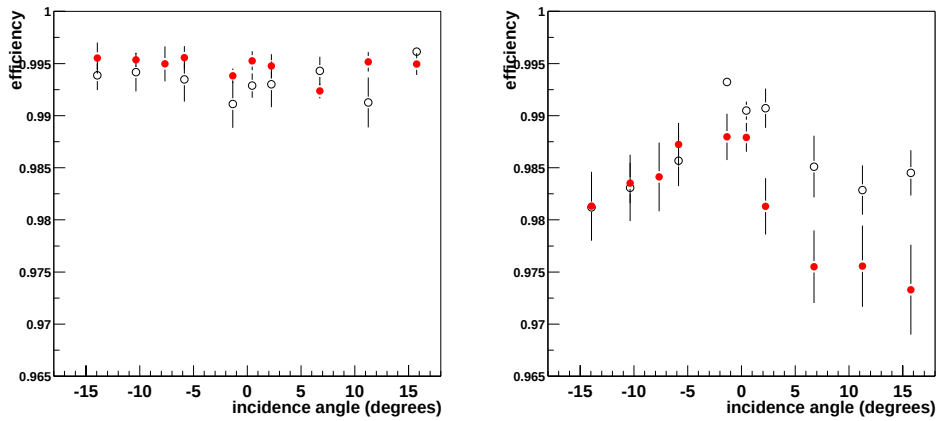

Fig. 18. Efficiency versus angle for non-irradiated modules at 1.2 fC (left) and irradiated at 1.2 fC (right). Filled markers are measurements in a 1.56 T magnetic field, open markers without field

pattern is seen in the irradiated modules. Although the errors are quite large [2] the efficiency clearly decreases with increasing incidence angle of modules. In the magnetic field the maximum is shifted to negative angles due to the Hall effect. The efficiency is close to or above 98 % in all cases.

The spatial resolution with binary readout depends on the number of strips in the cluster. The particle position will be better obtained if there is more

[2] Note that these are the standard deviation of the measurements for a certain angle for all the modules

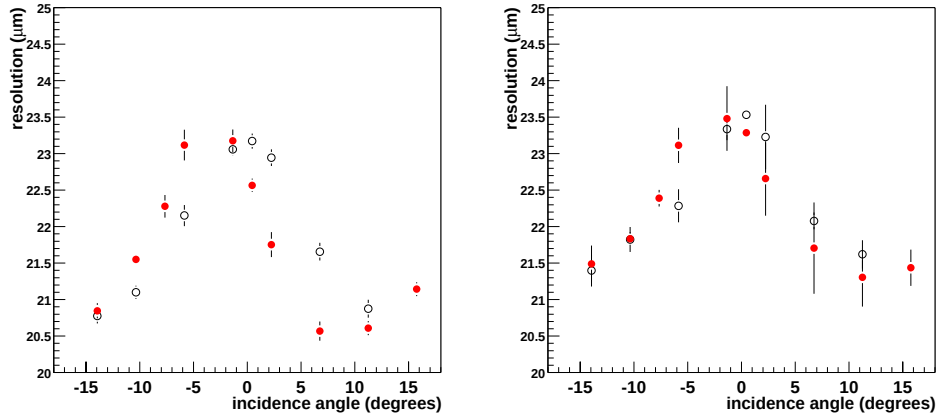

Fig. 19. Resolution in μm versus angle for non-irradiated modules at 1 fC (left) and irradiated at 1 fC (right). Filled marker are measurements in a 1.56 T magnetic field, open markers without field

than one strip with signal over threshold. At non-perpendicular incidence the fraction of events with signal in two strips (3 is very unusual) increases. So an improvement of the resolution with changing angle is expected. In Figure 15 left (non-irradiated) and right (irradiated) are the values of resolution versus angle. There difference between the worst (0°) and the best (±15°) resolution is around 2 μm. Again the magnetic field causes a shift.

12 Edge and gap measurements

In the ATLAS SCT there will be a small overlap between neighbouring modules. This will allow their relative alignment to be calculated from tracks which pass through the edge of both modules. It is therefore important that the detectors remain efficient at their edges, and that the residuals are not significantly distorted by edge effects in the detector electric field.

12.1 Edge

To investigate the behaviour of the modules near their edges, during the period 10th to 13th August 2001 some of the barrel modules were offset so that the beam passed through the corners of the detectors (as in Figure 20a), or in the gap between the detectors (Figure 20b).

Figure 21a shows the residuals as a function of the projected perpendicular position of the track from the center of the last strip. No significant deviation

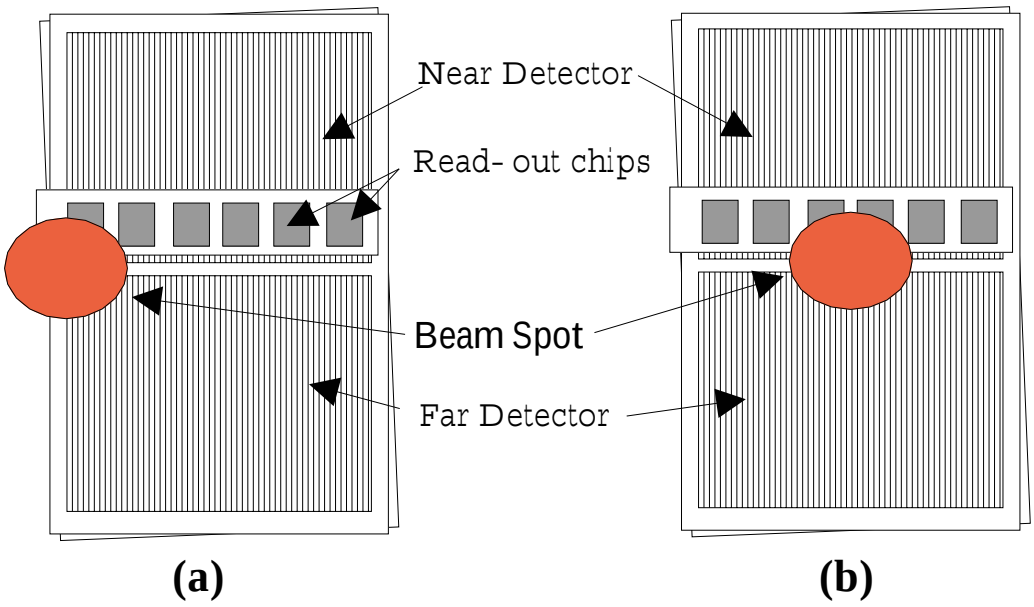

Fig. 20. The beam edge **(a)** and gap **(b)** positions.

from zero is observed for the tracks centered inside the middle of the last strip. The extreme left-hand bin records tracks with projected positions closest to the strip beyond the last read-out strip. These tracks have a low efficiency, since hits will not be detected unless they share charge into the neighbouring active strip. They will of necessity give rise to large residuals. It is therefore suggested that single-strip clusters on the first and last active strips are not used for module alignment.

The fall-off in efficiency near the edge of the detector is shown in Figure 21b. It can be seen that the module remains fully efficient to the center of the last read-out strip, beyond which the efficiency drops to zero over a distance about 40 μm. This is what one might expect, since beyond this point, the majority of the charge will lie on the final strip, which is not read out.

12.2 Gap

The module is not expected to be efficient in the gap between the two detectors. The size of this "dead area" was investigated for the modules with the beam in the corner position. Efficiency was measured as a function of the projected position of the track in the direction parallel to the strips.

The efficiency drop in the inactive region is shown for module 0029 in Figure 23. The size of the region, found by fitting a step function, smeared with a gaussian to each edge. The full width at half maximum of the fitted gap was

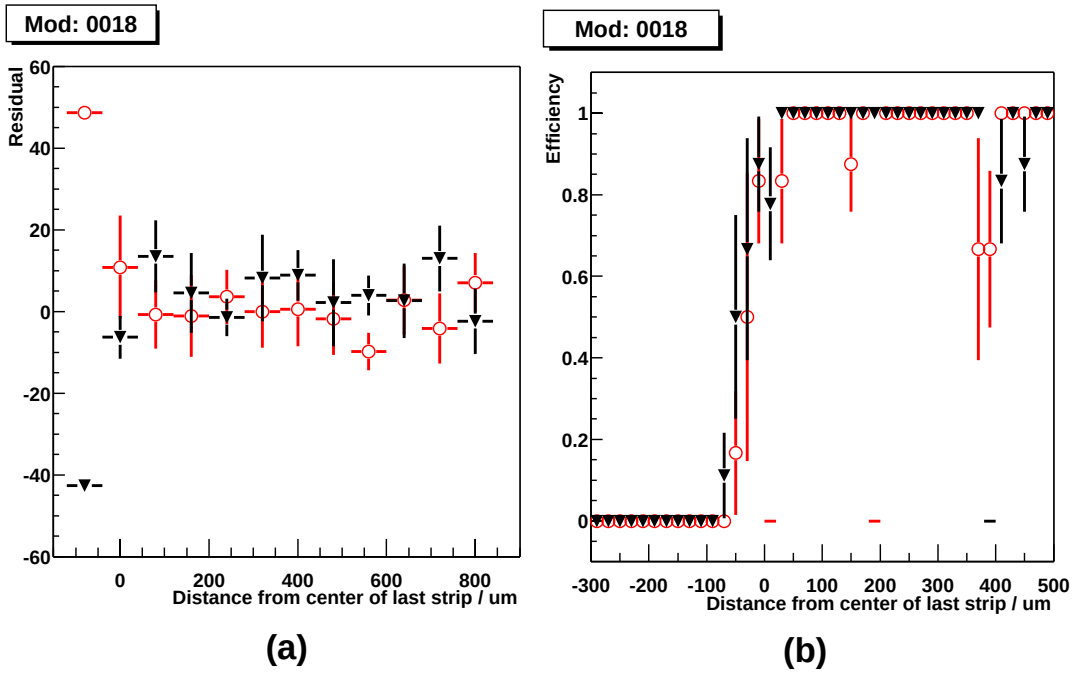

Fig. 21. Residuals **(a)**, and efficiency **(b)** of module 0018 as a funtion of the projected distance of the track from the center of the final read-out strip. The red circles (black triangles) correspond to link 0 (1), the different sides of the module. Note that the residuals beyond the edge of the module (those with negative distances) are calculated on approximately an order of magnitude less statistics than the others, but have a much smaller spread resulting in narrower error bars.

measured for each side of three modules, lying in the range 2038 to 2082 μm, with a mean of 2058 μm, which is consistent with what we expect. The expected dimensions of the dead area around the gap are shown in Figure 22. The total inactive distance is expected to be $130 + 2 \times 980 = 2090$ μm.

As shown in Figure 22, there is no metalisation over the end of the strip on the far detector because of the presence of a polysilicon biasing resistor. To investigate whether this might cause a decrease in efficiency near the end of the strips, the asymmetry in the sharpness of the rise- and fall-rates was measured. No significant asymmetry was measureable with the resolution and statistics available, since the fitted asymmetries were of the same order as their error of about 20 μm.

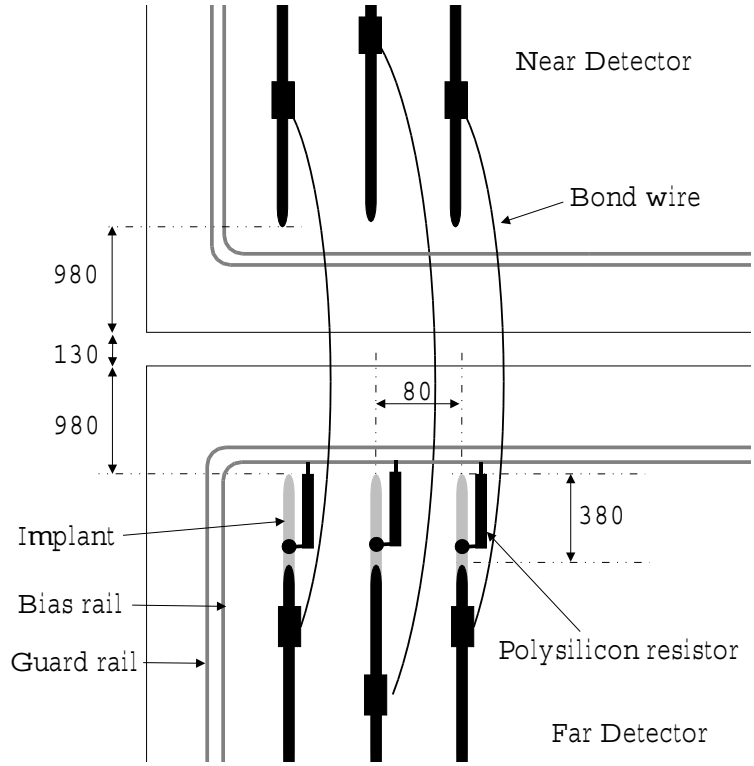

Fig. 22. Diagram of the corners of the two detectors, showing the dimensions of the gap between them (not to scale). The inactive area consists of the physical gap between the cut ends of the detectors plus the distance between the end of the strip implant and the cut end of each detector. All distances are in μm.

13 Pulse-shape analysis

When the charge measurements is repeated for a range of sampling times, the median pulse of the shaper can be reconstructed. In the laboratory the delay between generation of the charge and sampling can be controlled explicitly using the calibration circuit or a laser setup [15]. In asynchronous test beams this control is not possible, but the delay between the raw trigger and the clock is measured with a TDC. There is a basic difference between the measurement with the calibration circuit and the others. With the calibration circuit the influence of detectors in the pulse shape is avoided. Thus, the input to the shaper/amplifier electronics is very nearly a delta pulse.

The response of the shaper/amplifier of the ABCD chips to a delta pulse is given by [15]:

$$\begin{aligned} a(t) = &[5.26 \cdot 10^{-4} \cdot t^2 + 5.54 \cdot 10^{-4} t + 5.83 \cdot 10^{-3}] \cdot \exp(-0.1 \cdot t) \\ &-5.83 \cdot 10^{-3} \exp(-5 \cdot 10^{-3} \cdot t) \end{aligned} \quad (3)$$

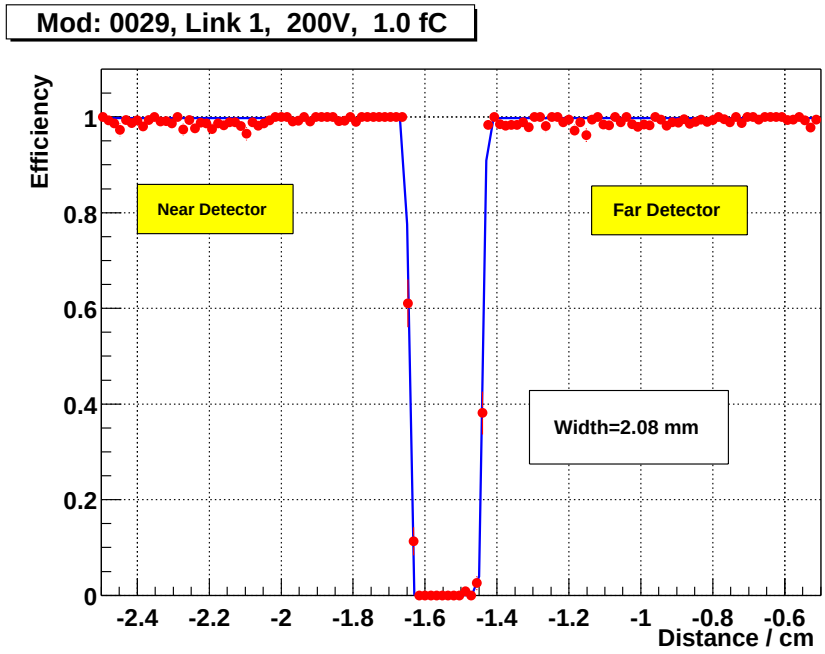

Fig. 23. The efficiency of module 0020 as a function of distance parallel to the strips, with a zero-point defined by the tracking telescope. The central inefficient region corresponds to the inactive area of the module, between detectors. The data were taken at 1.0 fC nominal threshold, with no magnetic field, with an applied bias of 200 V.

where t is time in ns. The input delta pulse is assumed to come at t=0. In order to describe the experimental data three fit parameters are needed: amplitude of the pulse, the start time of the pulse and the amplifier peaking time. The amplifier response function then becomes:

$$b(t) = A \cdot a\left(19.1\frac{t-d}{\tau_p}\right) \tag{4}$$

where A (amplitude), d (delay) and τ_p (peaking time of the electrons).

In the case of the beam test, the signal at the discriminator will be the time convolution of the collected detector signal and the amplifier-shaper time response. Therefore, the above function (delta pulse approximation) will be better with increasing voltages. In the following discussion, when beam test results on peaking times are reported, it should be interpreted as an effective peaking time due to the convolution of the detector signal and the electronics response.

Figure 24 shows an example of the response to the (fast) calibration pulse as obtained from strobe delay scans on two of the modules used in the august test beam. The figure on the left corresponds to a non-irradiated barrel module

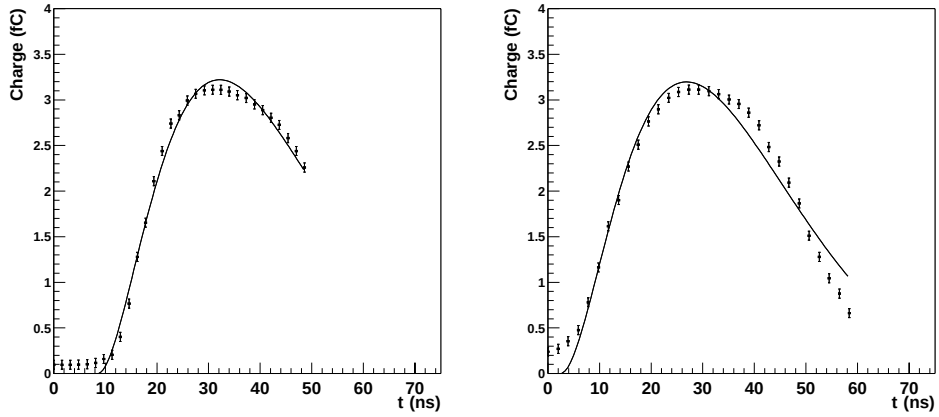

Fig. 24. Example of the reconstructed pulse shape done at the laboratory for two modules used at the August Test Beam, a non-irradiated (left) and a irradiated one (right).

and the one on the right to an irradiated module. The first thing to notice is that the continuous line (fit ABCD function) is not an exact description of the data. Especially the irradiated module shows a clear shoulder that can not be reproduced by the function. This effect is thought to be due to the overdrive needed by the comparator. When irradiation degrades the comparator the effect becomes more pronounced.

In asynchronous test beams [3] the pulse shape is reconstructed using the TDC information and the hit information from 3 time bins of the ABCD chip for being able to determine the median collected charge in a full range of 75 ns.

Two different approaches were used. In the first, the 50% points of the rise and fall in the efficiency versus time plot are found for a particular threshold, Q_{Th}. These points give the times after the particle arrival at which the median charge is equal to Q_{Th}. By varying this threshold, and plotting the times, we reconstruct the pulse shape (Figure 25). The points were fitted with the function of equation 3.

The second method divides the time range in 1 ns slices and fits the efficiency versus Q_{th} curve (s-curve) to obtain the median charge. In Figure 26 an example of the pulse shape for a non-irradiated (left) and an irradiated (right) modules with bias voltages 150 V and 350 V can be seen. No data with less than 0.7 fC has been taken for the fit. The lowest value measured in the test beam is 0.7 fC, so it makes no sense consider charges below. The fit for the non-irradiated module is very good, indicating that detector effects do not distort the pulse.

[3] In synchronous test beams an alternative method is available, see[9]

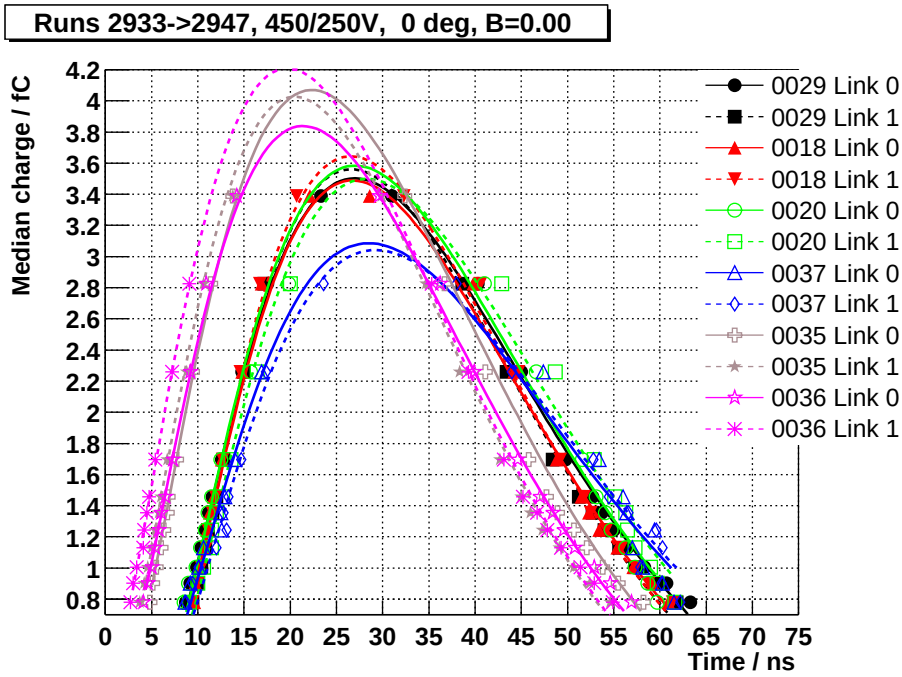

Fig. 25. Pulse shapes calculated from the 50% points of the efficiency–time graphs for particles at normal incidence and with no applied magnetic field. The applied bias was 450 V for the irradiated and 250 V for the non-irradiated module.

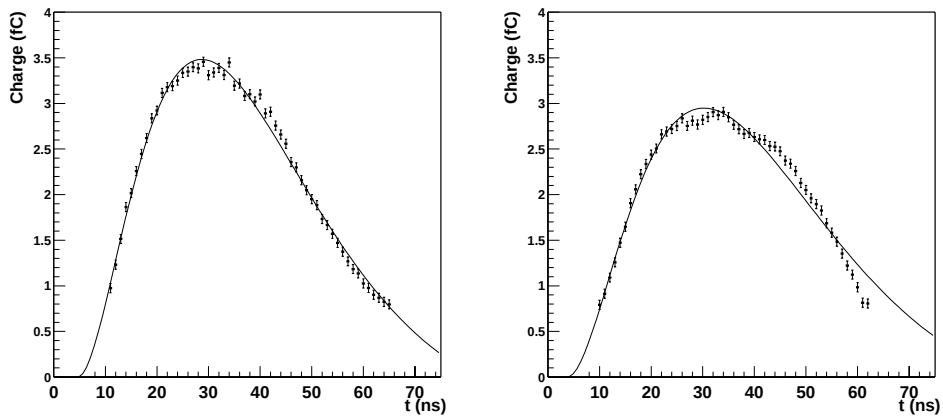

Fig. 26. Example of the reconstructed pulse shape done with test beam data for two modules, a non-irradiated (left) and a irradiated one (right) for bias voltages 150 V and 350 V.

As before, a shoulder appears in the irradiated module. This is true even for the highest bias voltage. As a result the fitted value of the peaking time is pushed up and will tend to overestimate the difference between non-irradiated and irradiated modules.

Table 5 is a summary of the peaking time results for barrel modules in the august test beam. The quoted errors are the standard deviation of the results from all modules. Results obtained with method 1 are listed with an asterisk (*) in the table.

non-irradiated			
bias voltage	150 V	250 V	250 V *
τ_p	23.1 ± 0.6	22.4 ± 0.5	21.8 ± 0.7
irradiated			
bias voltage	350 V	450 V	450 V *
τ_p	25.8 ± 0.7	25.5 ± 0.7	24.3 ± 0.7

Table 5
Effective peaking time of modules in the August beam test, results marked with * were obtained from the same data with the first method.

When the charge collection is affected by the operating conditions, like the bias voltage or the magnetic field, this will be reflected in the observed effective peaking time. Figure 27 presents the results obtained with method 2. The four kinds of markers represent the average over all the barrel modules present in the august test beam, divided into two groups. Round markers are results from non-irradiated modules an triangles the irradiated modules. The red markers are measurements in a 1.56 Tesla magnetic field, and the white ones without field.

Two different behaviours can be observed. In the non-irradiated modules, the peaking rises very steeply towards the lowest voltage, 100 Volts. This should be compared to the median charge vs bias results of figure 12. The explanation of the charge loss as a ballistic deficit of the shaper is confirmed here. When charge is collected more slowly, the amplifier responds with pulses of lower amplitude. At around 150 V the effect starts to soften out, and both median charge collected and peaking time become stabilised.

In irradiated sensors, the pn junction grows from the backplane (type inversion) and the field across the Silicon is very different. And indeed, the effect in irradiated modules is quite different, the peaking time is seen to decrease smoothly in the range from 300 to 450 Volts. The minimum peaking time obtained at 450 Volts is some 3 to 4 ns higher than the value obtained for non-irradiated modules at 250 Volts. Various effects can play a role here. The distortion of the shape - the shoulder - causes the fit function to return artificially high peaking times. The appearance of the shoulder in pulse shapes determined with the internal calibration circuit makes it plausible that this effect is due to the degraded power of the discriminator. The response of the shaper itself can also be slower. These are purely electronics effects and should

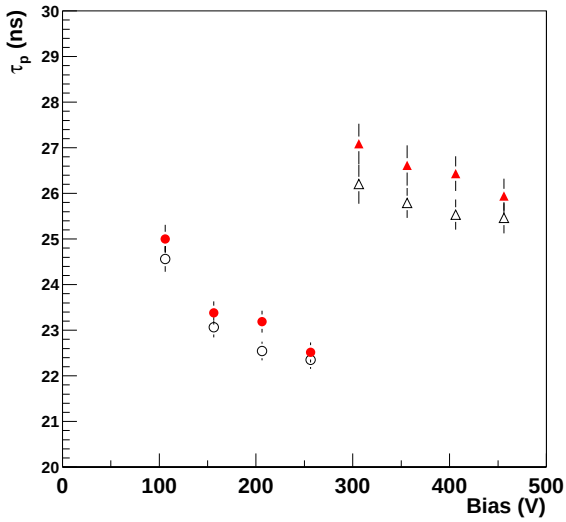

Fig. 27. Fitted peaking time vs bias voltage for all barrel modules in the august test beam. Results averaged over all non-irradiated (circle) and irradiated (triangles) modules without magnetic field (white) and in a 1.56 Tesla field (red). Perpendicular incidence.

not depend on the bias voltage. On the other hand, the structure of the detector signal is quite different in irradiated, type-inverted sensors. This has been studied in some detail in [16]. Simulations of the field in the Silicon indicate that the signal collection in over-depleted type-inverted is quite fast, but do not include effects due to formation of double junctions or detrapping of carriers. At this point the test beam results do not allow to disentangle between the various explanations. Valuable extra information could be obtained from test beam measurements of irradiated sensors read-out by non-irradiated electronics.

The data taken in a 1.56 Tesla magnetic field seems to indicate a slightly higher peaking time compared to the results without field, especially so for the irradiated modules. The results are compatible within errors, though, and further study is needed.

All barrel modules in the August test beam were populated with chips from one batch. The modules that were tested in October, however, were built with chips from a new batch, where the epitaxial layers were from a new vendor. Comparison between the two groups of modules allows to evaluate the combined effect of batch-to-batch variations and the change of vendor. The two irradiated modules built with these new chips showed a considerably higher noise occupancy, see table 3, in agreement with previous laboratory measurements. Table 6 shows a summary of the peaking time results for both types of chips. Comparing with table 5 it can be seen that the peaking time

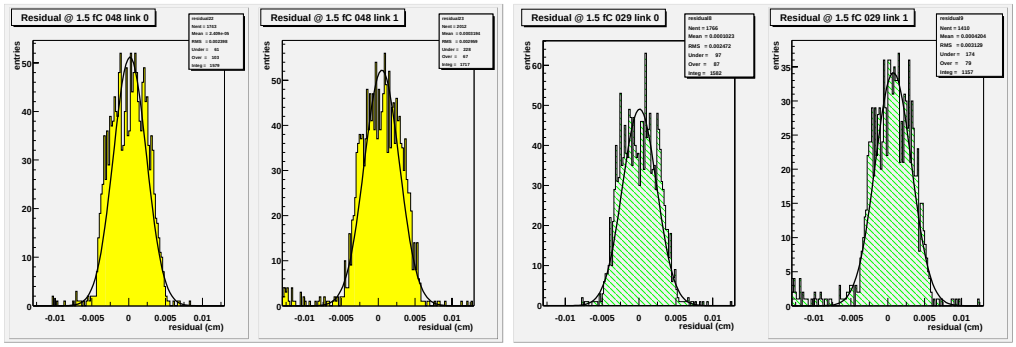

Fig. 28. Residuals of plane 0 and 1 for KB module 0048 (*left*) and barrel module 0029 (*right*).

of the new-epi chips is lower than the old epi by about 2 ns.

	non-irradiated	*irradiated*
bias voltage	150 V	350 V
τ_p	20.9 $\pm$ 1.3	23.7 $\pm$ 0.5

Table 6
Peaking time of modules in the October test beam

14 The KB module

The possibility of building an endcap module based on the barrel hybrid – hence named "KB" – assembled in an end-tap configuration with the endcap detectors, was considered by the SCT collaboration as a possible backup option after problems with the baseline K4 modules.

A first prototype (KB_0048) was successfully built by the CERN and Geneva groups in August 2001. In this first prototype, four W31 type wafers were used instead of W31-W32 pairs to enable use of an existing barrel pitch adapter. This module was thus built with a total strip length $\approx$ 8 mm longer than for the baseline outer endcap module. After electrical tests and standard characterization KB_0048 was included in the October 2001 testbeam.

The KB module performance was satisfactorily within SCT module specifications and similar to the barrel modules: the spatial resolution is 23 mm on both sides (see figure 28), the efficiency at 1 fC is higher than 99% and the noise occupancy is lower than 10^{-5} (see figure 29).

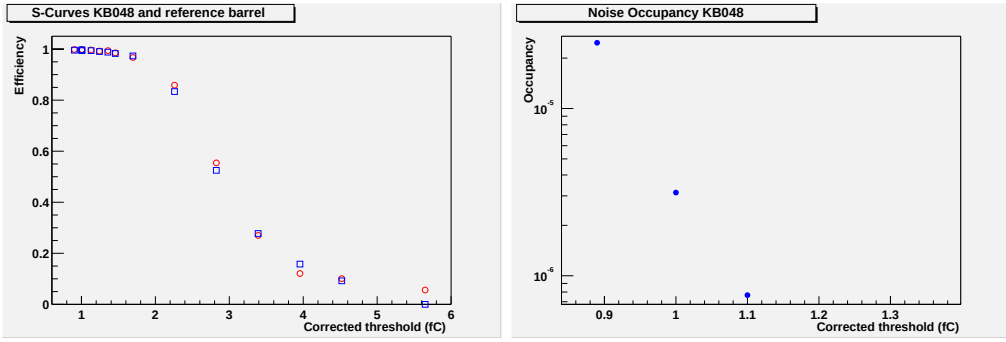

Fig. 29. *Left*: S-Curve KB module (circle) and reference module b029 (square). The calibration factor is applied to both modules. *Right*: Noise Occupancy of the KB module

References

[1] ATLAS Technical Proposal, CERN/LHCC/94-43 (1993)

[2] The ATLAS Semiconductor Tracker (SCT), http://atlas.web.cern.ch/Atlas/GROUPS/INNER_DETECTOR/SCT

[3] A.Barr et al., Beamtests of Prototype ATLAS SCT Modules at CERN H8 in June and August 2000, ATLAS Internal Note ATL-INDET-2002-005

[4] ATLAS/SCT Module and Hybrid Test DAQ http://atlas.web.cern.ch/Atlas/GROUPS/INNER_DETECTOR/SCT/testdaq/testdaq.html

[5] W. Dabrowski et al., Progress in development of the readout chip for the ATLAS semiconductor tracker. 6th Workshop on Electronics for LHC Experiments.

[6] Valencia SCT: DACs vs Temperature on ABCD3T http://alpha.ific.uv.es/sct/activities/electronics/dactempdep/

[7] The Valencia offline web page, http://ific.uv.es/sct/tb01/tb01.html; The Prague CU offline web page, http://www-ucjf.troja.mff.cuni.cz/~sct/tb

[8] DSTs, /castor/cern.ch/atlas/testbeam/sct/2001/dst_2/dstxxxx.root

[9] A.Barr et al., Performance of ATLAS SCT modules used as a fast binary telescope during LHC-structured beam at the CERN SPS, ATLAS Internal Note in preparation.

[10] T.Lari, Lorentz angle variation with electric field for ATLAS silicon detectors. ATL-INDET-2001-004

[11] V. Bartsch et al., An algorithm for calculating the Lorentz angle in silicon detectors. CMS IN-2001/027

[12] C. Leroy et al., Study of charge transport in non-irradiated and irradiated silicon detectors. Nucl. Inst. and Meth. A 426 (1999) 99-108

[13] T. J. Brodbeck et al., Carrier mobilities in irradiated silicon, ROSE/TN/2000-09

[14] V. Eremin ang Z. Li, Nucl. Inst. and Meth. A 362 (1995) 338

[15] S.Gadomski, P.Reznicek, Measurement of amplifier pulse shapes in SCT modules using a laser setup. ATL-INDET-2001-010

[16] T. Akimoto et. al., Beam study of irradiated ATLAS-SCT prototypes Proceedings of the 5th Florence conference, accepted in Nucl. Inst. and Meth. A.